Progress In Electromagnetics Research C, Vol. 114, 97–112, 2021

Multi-Objective Optimal Design of the MFW-IPM Machine for Improve Flux-Weakening Ability

Xiping Liu, Gaosheng Guo*, Wenjian Zhu, and Longxin Du

Abstract—In this paper, a novel mechanical-flux-weakening interior permanent magnet (MFW-IPM) machine is proposed to improve flux-weakening ability. The key of the proposed machine is that the permanent magnet is rotatable, and a mechanical device is equipped on both sides of the rotor. The mechanical device can regulate the air-gap magnetic field by rotating PM to change the leakage flux and magnetization direction of PM. As a result, the flux-weakening ability is improved. The flux-weakening principle of the MFW-IPM machine is investigated in detail. In addition, a multi-objective optimization method is adopted to improve the performance of the proposed machine. Then, the electromagnetic performances of the original machine and optimized machine are compared by finite element analysis. Finally, both simulation results and experimental tests verify the effectiveness of the flux-weakening enhancement design and optimization method.

1. INTRODUCTION

Permanent magnet synchronous motors (PMSMs) have been widely applied in household appliances, new energy power generation, electric vehicles, aerospace industry, and other fields [1–3], because they offer significant advantages such as high efficiency, high torque-to-volume ratio, and high power factor [4, 5]. Especially in the field of automobiles, pure electric vehicles (EV) gradually replace traditional fuel vehicles due to their significant advantages of high efficiency and zero-emission [6]. However, the air-gap magnetic field of conventional PMSM is difficult to regulate, which limits its speed range [7]. Generally, negative d-axis flux-weakening current is applied to weaken the magnetic field [8], but it inevitably affects the efficiency and increases the risk of PM irreversible demagnetization [9, 10].

To solve this problem, some methods have been proposed. In [11, 12], hybrid excitation machines are proposed, incorporating both PMs and field windings. Those machines can achieve controllable flux by controlling the amplitude of the field current. However, the use of field windings to enhance or weaken the air-gap magnetic field inevitably increase copper loss and reduce the efficiency of the machines. In [13, 14], some flux-intensifying permanent magnet (FI-PM) machines are proposed. This type of machine possesses the unique characteristic of d-axis inductance L_d larger than that of q-axis inductance L_q. It means that the machines can obtain the maximum torque at a positive d-axis current [15], so the risk of PM irreversible demagnetization is reduced [16]. The characteristic can improve the flux-weakening ability of the machine. Nevertheless, a large current is still needed for flux-weakening [17]. In [18], a variable flux memory motor (VFMM) is proposed. Since the low coercive-force (LCF) PM is applied in VFMM, the LCFPM magnetization strength of LCFPM can be controlled by injecting d-axis current pulses to remagnetize or demagnetize [19]. The flux controllability of VFMM can be easily achieved to widen the speed range. However, the motor needs to add the corresponding control system to control the magnetization state of the PM, thus the cost will increase.

Received 3 June 2021, Accepted 23 July 2021, Scheduled 29 July 2021
* Corresponding author: Gaosheng Guo (1400681644ggs@gmail.com).
The authors are with the School of Electrical and Automation, Jiangxi University of Science and Technology, Ganzhou, China.

This paper proposes a novel MFW-IPM machine. The proposed machine is equipped with a mechanical flux-adjusting device, and the PM adopts a cylindrical permanent magnet (CPM). The mechanical device is driven by centrifugal force to rotate the CPM, thus weakening the air-gap magnetic field. This method can effectively widen the speed range and reduce the injection of flux-weakening current. Generally, the motor needs better torque performance and flux-weakening ability to satisfy the requirement for industrial applications. How to meet these requirements has become a problem in the process of machine design.

To obtain a satisfactory performance of machines, multi-objective optimization methods have been widely applied in recent research [20–22]. In [23], multi-objective optimization based on a nondominated sorting genetic algorithm (NSG-II) is adopted to optimize the selected key parameters of the machines. In [24], the structural parameters of the motor are optimized by adopting dual-level response surface methodology and Booth's algorithm. In [25], an IPMSM is optimized by combining a genetic algorithm (GA) with the coarse mesh finite element method. These optimization methods can effectively improve the performance of the motor.

In this paper, the topology and flux-weakening principle of the MFW-IPM machine are introduced in Section 2. In Section 3, to improve the operational performances of the proposed machine, the multiple objective genetic algorithm (MOGA) is utilized to optimize the objectives of output torque, torque ripple, and flux-weakening ability. In Section 4, the electromagnetic characteristics of the original and optimized machines are compared. In Section 5, a prototype of the proposed motor is manufactured according to the optimization results. The testing results of the prototype show that the design of flux adjustment is effective as well as a satisfactory consistency between experimental data and theoretical predictions. Finally, some conclusions are drawn in Section 6.

2. MODEL TOPOLOGY AND OPERATION PRINCIPLE

2.1. Model Topology

The topology structure of the MFW-IPM machine is shown in Figure 1. The stator has 48 slots with integral slot distributed windings. It can be seen that the PM of the proposed machine adopts CPM. The assembly drawing of the proposed machine is shown in Figure 2. In Figure 2, it can be observed that the mechanical device is mounted on both sides of the rotor. The mechanical device mainly consists of a disc, spring, sliding block, gear, and connecting rod. From the two figures, it can be seen that one end of the spring is fixed to the disc and the other end connected to the slider. The disc is provided with a chute for the sliding block to move. Moreover, one end of the connecting rod is fixed on the gear and the other end embedded in the center position of the permanent magnet, so the rotating gear drives the permanent magnet around the central axis. Besides, the corresponding key parameters of the motor are listed in Table 1.

Table 1. Key parameters of the motor.

Parameters	Value
Stator outer diameter	269.6 mm
Rotor outer diameter	160.4 mm
Stack length	40 mm
Rated power	1.2 kW
Number of slots/poles	48/8
Rated voltage	40 V
Rated speed	750 rpm
Output torque	$\geq$ 16 Nm
PM material	NdFe35

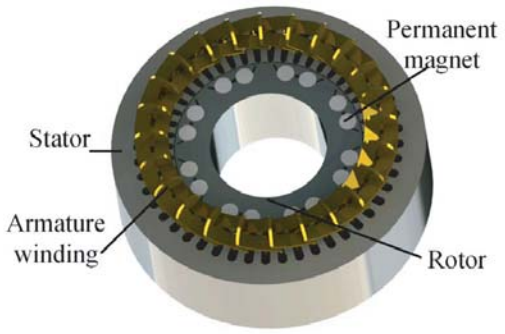

Figure 1. Topology of the machine.

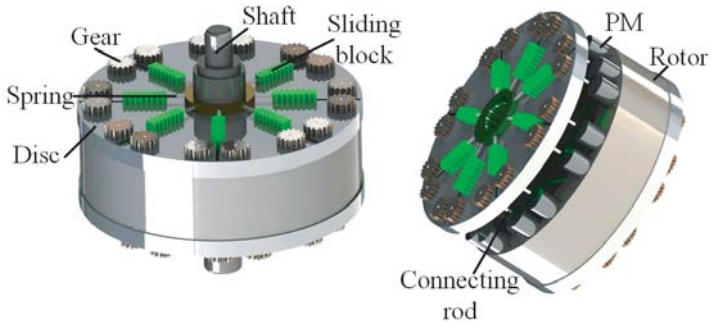

Figure 2. Assembly drawing of the machine.

2.2. Operation Principle

The variable flux of the MFW-IPM machine is achieved by the mechanical flux-adjusting device. As the speed increases, the slider is subjected to greater and greater centrifugal force, and the slider moves along the chute; when the speed reaches the base speed, the slider touches the gear; as the speed continues to increase, the slider pushes the gear to rotate, thus driving the permanent magnet to rotate. The rotation angle of CPM is defined as α.

To better analyze the variable flux principle, the two states of rotation angle α of 0 deg and 40 deg are analyzed. The flux path of the MFW-IPM machine under different α is shown in Figure 3. Comparing Figures 3(a) and (b), it can be found that the leakage flux of the MFW-IPM machine increases with the increase of α. Moreover, since CPM rotates around the central axis of the PM, the rotation of the CPM can be regarded as the magnetization direction of the CPM rotates around the central axis of the PM, which means that the included angle between the magnetization direction of the CPM and the initial magnetization direction of the CPM is equal to α. Based on the above analysis, it can be seen that the flux-weakening of the proposed machine is realized by increasing the leakage flux of the CPM and changing the magnetizing direction of the CPM.

Furthermore, the simplified equivalent magnetic circuit of the MFW-IPM machine is shown in Figure 4, where F_s and F_{pm} are the magnetomotive forces (MMFs) of the stator and PM. R_s, R_r, R_g, R_δ, R_{pm} are the reluctances of stator, rotor, air gap, bypass of leakage flux, PM. ϕ_s, ϕ_{pm}, ϕ_δ are the magnetic fluxes of stator and PM, bypass of leakage flux. ϕ_δ can be expressed as:

$$\begin{cases} \begin{bmatrix} \phi_s \\ \phi_{pm} \end{bmatrix} = \dfrac{A}{|A|} \begin{bmatrix} F_s \\ F_{pm} \end{bmatrix} \\ A = \begin{bmatrix} R_\delta + R_{pm} & 2R_\delta \\ R_\delta & R_r + R_s + R_g + 2R_\delta \end{bmatrix} \\ |A| = (R_\delta + R_{pm})(R_s + R_g + R_r) + 2R_{pm}R_\delta \end{cases} \tag{1}$$

$$\begin{cases} \phi_\delta = \phi_{pm} - \phi_s \\ = \dfrac{(R_g + R_g + R_s) F_{pm} - R_{pm}F_s}{2R_\delta R_{pm} + (R_\delta + R_{pm})(R_r + R_s + R_g)(R_r + R_s + R_g)} \end{cases} \tag{2}$$

The rotation of the CPM has a great effect on R_δ. As the rotation angle α increases, R_δ decreases. According to Equation (2), it can be observed that with the decrease of R_δ, ϕ_δ increases correspondingly.

Figure 5 shows the variation diagram of the flux linkage ψ_{pm} with the rotational angle of CPM α. It can be observed that as α increases, ψ_{pm} decreases faster and faster. When α reaches the boundary angle $\alpha_{\max}$, ψ_{pm} reaches its minimum. The variation characteristics of $\psi_{pm}(\alpha)$ can be expressed as:

$$k(\alpha) = \frac{\partial \psi(\alpha)}{\partial \alpha} \quad (0 \le \alpha \le \alpha_{\max}) \tag{3}$$

$$\psi_{pm}(\alpha) = \psi_{pm\_0} + \int_0^\alpha k(\alpha) d\alpha \tag{4}$$

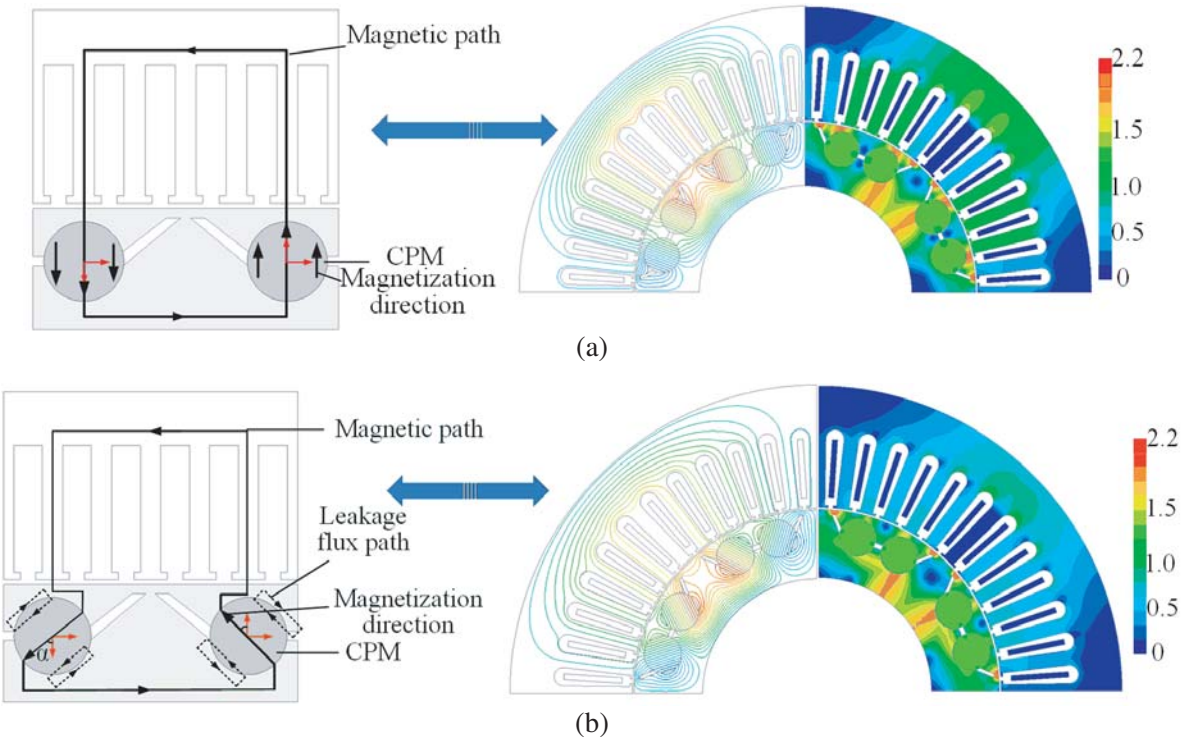

Figure 3. Flux path of the MFW-IPM machine under different α. (a) $\alpha = 0$ deg. (b) $\alpha = 40$ deg.

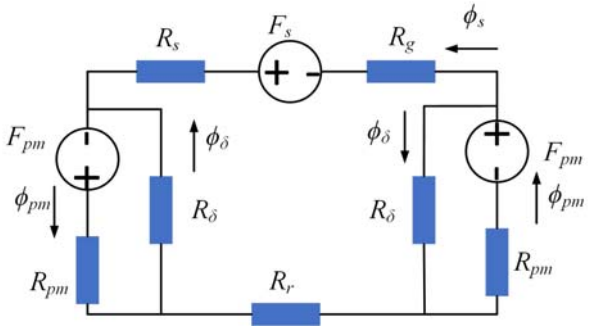

Figure 4. Simplified equivalent magnetic circuits of the MFW-IPM machine.

According to Equation (4), the maximum angular speed $\omega_{\max}$ of the proposed motor can be expressed as (ignore the phase resistance):

$$\omega_{\max} = \frac{U_{lim}}{p(\psi_{pm}(\alpha) - L_d I_{lim})} \tag{5}$$

where U_{lim} and I_{lim} are the limit values of voltage and armature current, respectively, and p is the number of pole pairs. According to Equation (5), the speed range of the machine increases as the flux linkage $\psi_{pm}(\alpha)$ decreases.

3. MULTI-OBJECTIVE OPTIMIZATION

3.1. Optimization Process

To improve the performances of the MFW-IPM machine, the optimization of the proposed machine is necessary. The multi-objective optimization flowchart of the MFW-IPM machine is described in

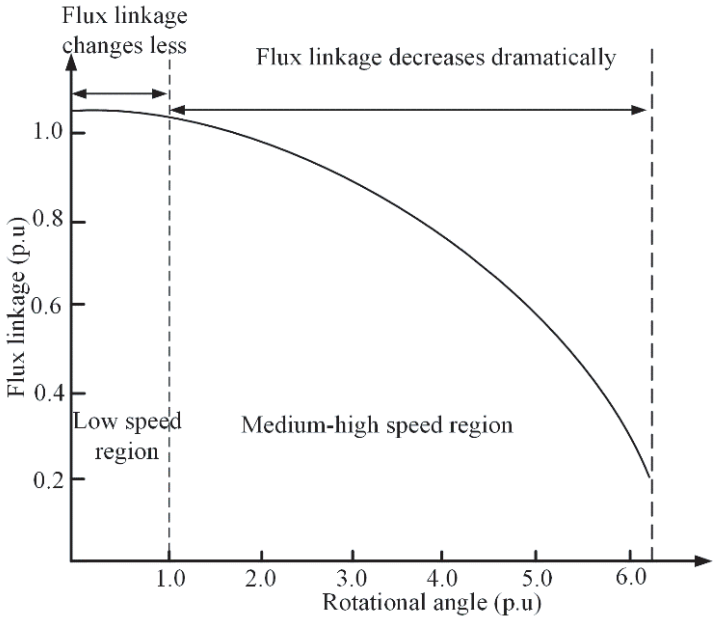

Figure 5. Variation diagram of the flux linkage ψ_{pm} with the rotational angle of CPM α.

Figure 6, which contains the following steps:

Step 1: Initial design of MFW-IPM machine. According to the design theory of the IPMSM and the design requirements of the proposed machine, the dimensions of the initial specifications of the MFW-IPM machine can be obtained. The design variables are selected to establish the parametric model. Besides, according to application requirements, the optimization objectives are determined.

Step 2: Parameters sensitivity analysis. The sensitivity $S(x_i)$ of each selected design variable on optimization objectives is defined. Then, the design variables are divided into two layers based on the values of the corresponding sensitivity.

Step 3: Multi-objective optimization. The optimization model of the MFW-IPM machine is presented. Based on the above results of sensitivity analysis, the strong sensitivity design variables are selected to be the final design variables. The MOGA optimization method is adopted to determine the final value of the design variables.

Step 4: Performance analysis. In this section, the electromagnetic performance comparison of the original and optimized MFW-IPM machines is analyzed to verify the optimization process. Finally, the experiment simulation is carried out to verify the electromagnetic performance of the MFW-IPM machine.

Table 2. Variation range of the design variables.

Design variables	Variation ranges
Outside Magnetic bridges radius R_{om} (mm)	$[77, 79]$
Outside Magnetic bridges angle α_o (deg)	$[20, 70]$
Inside magnetic barrier width W_{im} (mm)	$[1, 5]$
PM diameter R_{pm} (mm)	$[14.5, 16.5]$
Distance between PMs D_{pm} (mm)	$[18, 26]$
PM height H_{pm} (mm)	$[68, 70]$
Outside magnetic barrier width W_{om} (mm)	$[1, 6]$

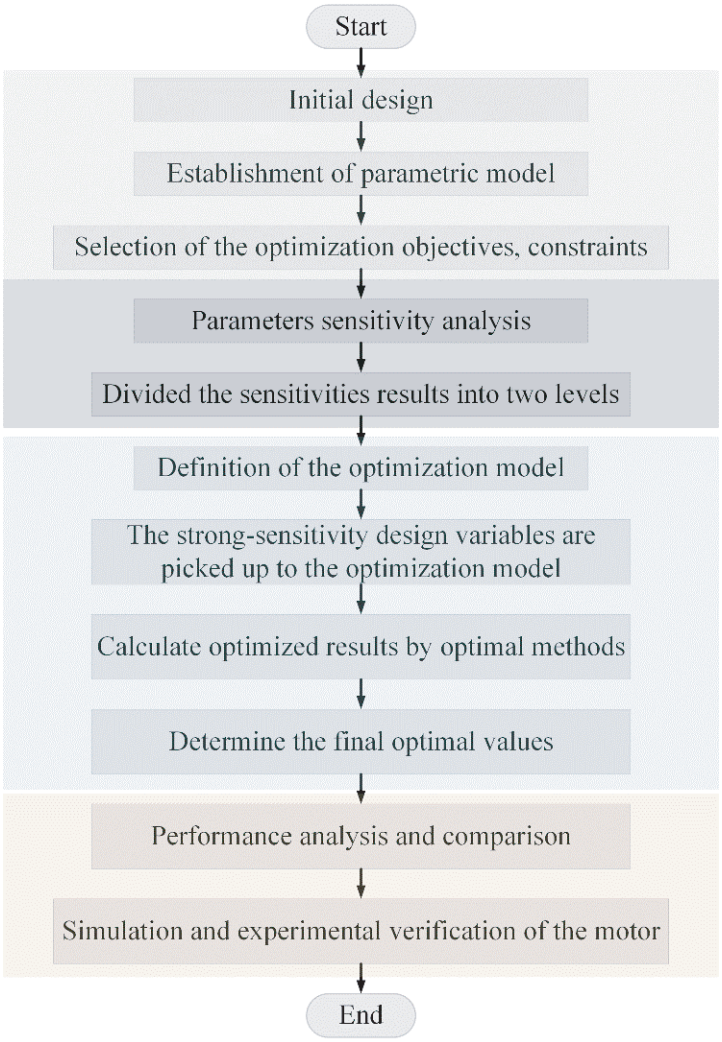

Figure 6. Flowchart of multi-objective optimization.

3.2. Deterministic Optimization Requirements

The parametric models of the proposed motor are shown in Figure 7, with some key parameters as the design variables. The selected variables and corresponding variations are listed in Table 2. The

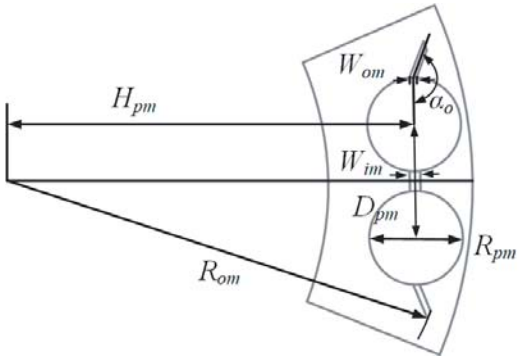

Figure 7. Parametric model of the machine.

optimization objectives are selected based on the performance requirements of the machines in the application. In order to meet the proposed motor in the rated operating state of high output torque, the torque of the motor is selected as an optimization objective. To realize the stability of motor operation, the torque ripple needs to be optimized. In addition, to improve the flux-weakening ability of the machine, the flux-regulating ratio is selected as a design objective. Thus, the torque, torque ripple, and flux-regulating ratio are selected as the optimization objectives in this section.

3.3. Comprehensive Sensitivity Analysis

A comprehensive sensitivity method is adopted to recognize the influence of the design parameters in optimization objectives effectively, and the corresponding sensitivity index is defined as

$$S_{(x_i)} = \frac{V(E(y|x_i))}{V(y)} \tag{6}$$

where y is the optimization objective, x_i $(i = 1, 2, 3 \ldots n)$ the selected design variables, $E(y/x_i)$ the average value of y when x_i is constant, $V(E(y/x_i))$ the variance of $E(y/x_i)$, and $V(y)$ the variance of y. A positive sensitivity index indicates that the optimization objective will increase with the design variable increases, whereas a negative one means a contrary variation. A greater absolute value of the sensitivity index means that the design variable has more impact on the optimization objective. According to Equation (6), the sensitivity index of each variable on the optimization objectives can be calculated and shown in Figure 8. From the figure, it can be seen that most of the design variables have obvious effects on the optimization objectives. Then, the design variables are divided into two levels according to the sensitivity value of each variable and listed in Table 3. The strong-sensitivity design variables are selected as the final variable to improve the optimization efficiency.

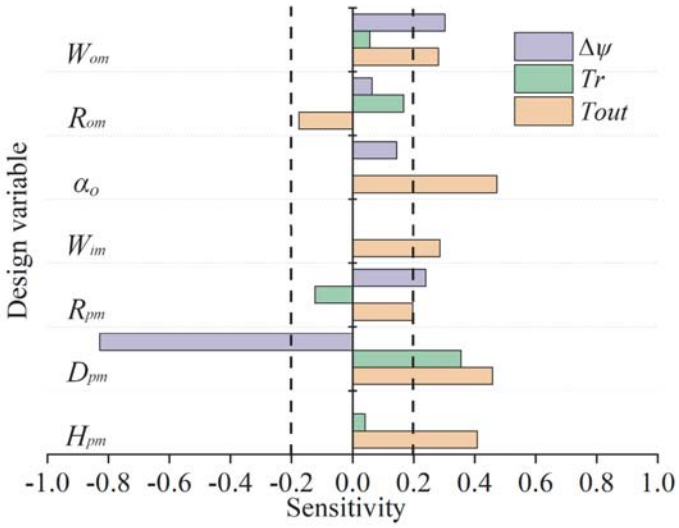

Figure 8. Sensitivity analysis.

Table 3. Classification of the design variable.

Motor	Classification	Design variables
MFW-IPM	Level 1:Weak-sensitivity	R_{om}
	Level 2:Strong-sensitivity	W_{om}, α_o, W_{im}, R_{pm}, D_{pm}, H_{pm}

3.4. Multi-Objective Optimization

In the above section, optimization objectives and variables are identified. In order to obtain satisfactory motor performance, the trade-off objective function of the MFW-IPM machine is presented as follows:

$$f(x_i)_{\min} = w_t \frac{T'_{out}(x_i)}{T_{out}(x_i)} + w_r \frac{T'_r(x_i)}{T_r(x_i)} + w_f \frac{\Delta\psi'(x_i)}{\Delta\psi(x_i)} \tag{7}$$

The boundary constraints of the MFW-IPM machine are

$$\begin{cases} T_{out} \geq 16\,\text{Nm} \\ T_r = \dfrac{T_{out\_\max} - T_{out\_\max}}{T_{out}} \times 100\% \leq 15\% \\ \Delta\psi = \dfrac{\psi_{pm}(\alpha = 0\,\text{deg}) - \psi_{pm}(\alpha = 40\,\text{deg})}{\psi_{pm}(\alpha = 0\,\text{deg})} \geq 40\% \end{cases} \tag{8}$$

where x_i is the design variables; $T'_{out}(x_i)$, $T'_r(x_i)$, $\Delta\psi'(x_i)$ are the initial values of output torque, torque ripple, flux-regulating ratio, respectively; $T_{out}(x_i)$, $T_r(x_i)$, $\Delta\psi(x_i)$, are the optimized values; $T_{out\_\max}$ and $T_{out\_\min}$ are the maximum and minimum of the output torque; w_t, w_r, w_f are the weight coefficient of the three optimization objectives. With considering the importance of optimization objectives in evaluating motor performance, the weight coefficients are set as 0.2, 0.4, 0.4, respectively. The MOGA is adopted for the MFW-IPM machine to achieve a tradeoff design. The optimization result of the MFW-IPM machine is shown in Figure 9, where the optimal point can be obtained efficiently based on the boundary constraints. The optimization results of the design variables of the proposed machine are listed in Table 4.

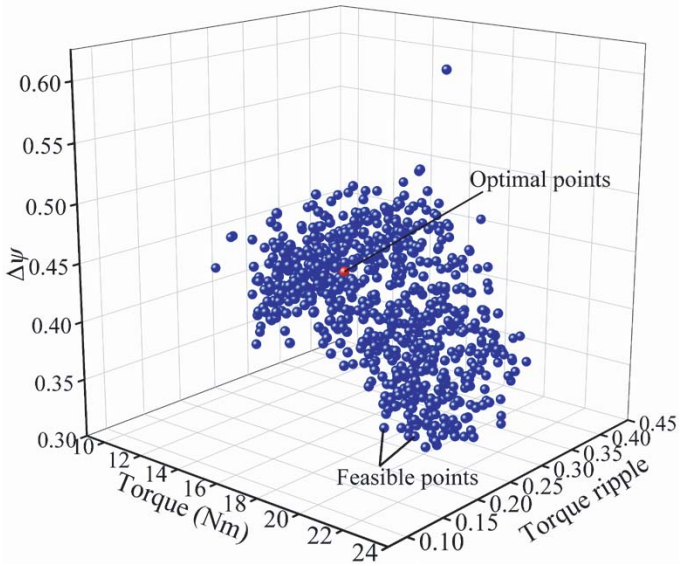

Figure 9. Optimization results of the machine.

4. COMPARISON OF MOTOR PERFORMANCE BEFORE AND AFTER OPTIMIZATION

4.1. Flux Distribution

The flux linkage of the original and optimized machines under no-load is shown in Figure 10(a). It can be seen that the flux linkages of the two machines are nearly identical. It means that the PM utilization of the two motors is the same with a similar PM torque. Moreover, Figure 10(b) shows the flux linkages

Table 4. Optimization results of the design variables.

Design variables	Initial values	Optimal values
W_m	2 mm	1.216 mm
α_o	40 deg	50.863 deg
W_{im}	3 mm	4 mm
R_{pm}	16.4 mm	16.431 mm
D_{pm}	20 mm	9.287 mm
H_{pm}	69 mm	69.933 mm

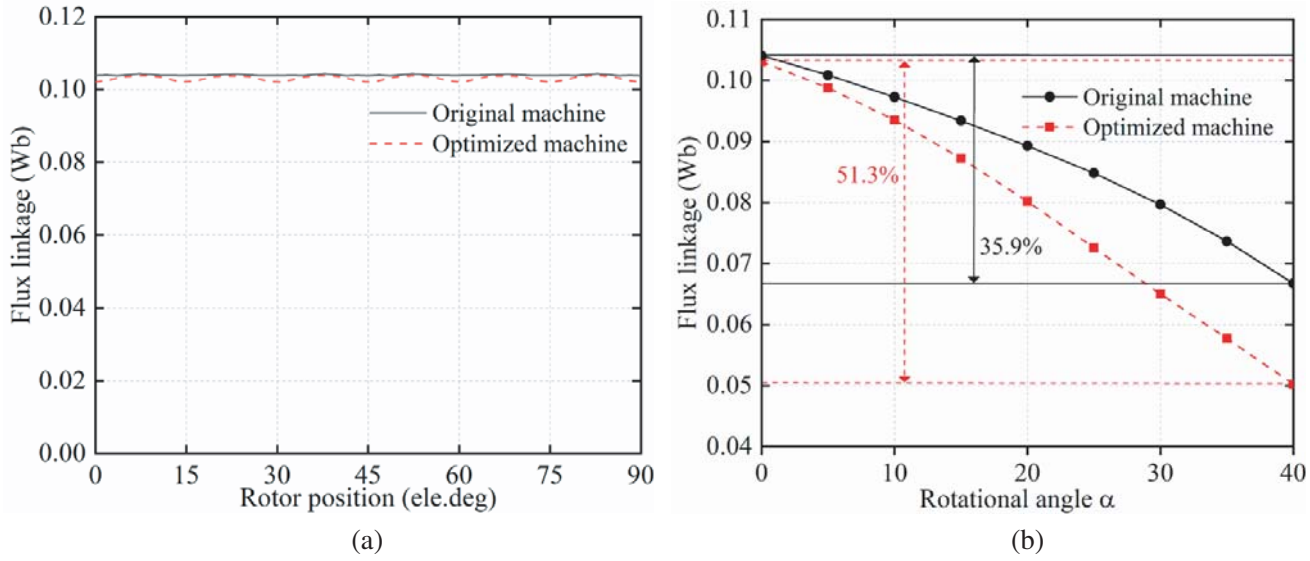

Figure 10. Flux characteristic. (a) The flux linkage under different rotor positions. (b) The flux linkage under different rotational angles α.

of the original and optimized motors at different rotational angles α, and it can be observed that the flux linkage decreases as the rotational angle α increases. The range of flux variation of the optimized machine is about 51.3%, which is larger than that of the original machine of 35.9%. It means that the variable flux characteristic of the optimized motor is better and verifies the effectiveness of the optimization method.

4.2. No-Load Back-EMF

In Figure 11(a), the back electromotive force (EMF) waveforms of the original machine and optimized machine at the speeds of 750 rpm (α = 0 deg), 3000 rpm (α = 40 deg) are shown. It can be found that the peak values of the back-EMF of the two motors are nearly identical at the speed of 750 rpm. However, at the speed of 3000 rpm, the peak value of the optimized machine is smaller than that of the original machine due to the lower value of flux linkage. Besides, the corresponding harmonic analysis of the four back-EMFs is shown in Figure 11(b). At the rotational angle α of 0 deg, it can be seen that the values of the fundamental waves of the optimized machine and original machine are nearly identical, and the value of the three-order harmonic of the optimized machine is slightly lower than that of the original machine. At the rotational angle α of 40 deg, the total harmonic distortion of the optimized machine about is 9.9%, which is lower than that of the original machine of 15.2%. It means that the optimized machine has a relatively more sinusoidal back-EMF waveform.

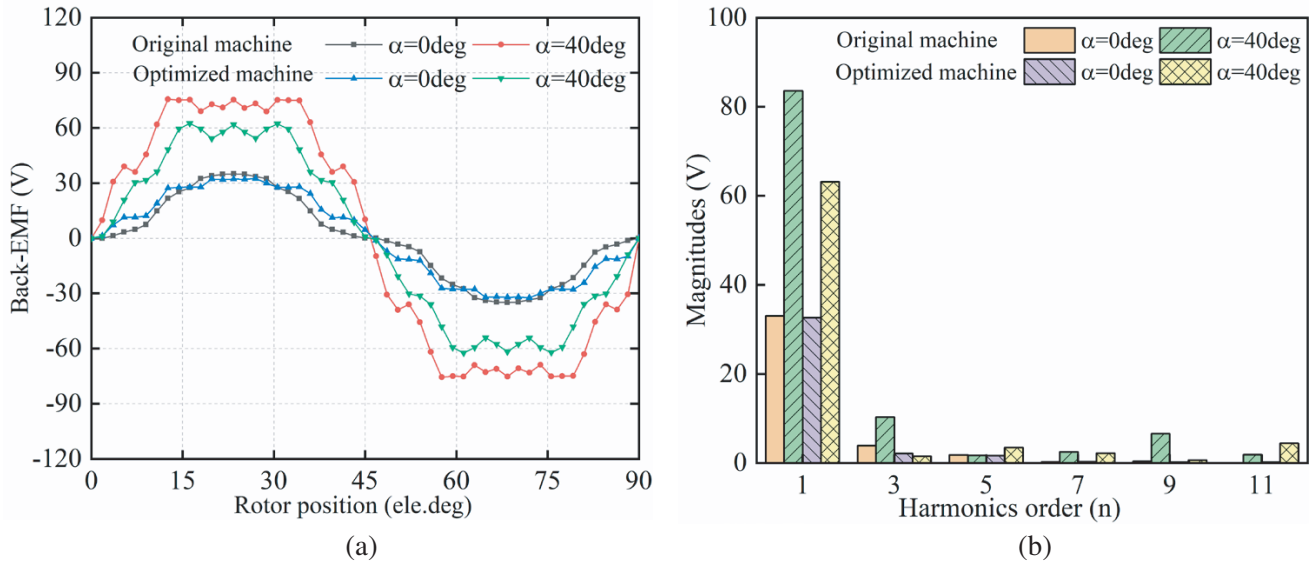

Figure 11. Comparison of no-load back EMF under different α. (a) Waveforms. (b) Spectral component.

4.3. Inductance Characteristics

Inductance has an effect on both reluctance torque and flux-weakening capability, so it is necessary to analyze the inductance characteristic. Figure 12 shows the inductance characteristic of the MFW-IPM machine, with the current of 25 A. In Figure 12(a), the inductance as a function of the current angle and rotation angle of PM is shown. As seen from the figure, L_d and L_q of the optimized machine are larger than that of the original machine. Moreover, the difference between L_q and L_d of the MFW-IPM as a function of the current angle and rotation angle of PM is shown in Figure 12(b). The difference between L_q and L_d of the optimized machine is for the most part greater than that of the original motor. However, when the rotational angle α is greater than 30 degrees, the difference between L_q and L_d of the optimized machine is smaller than that of the original motor.

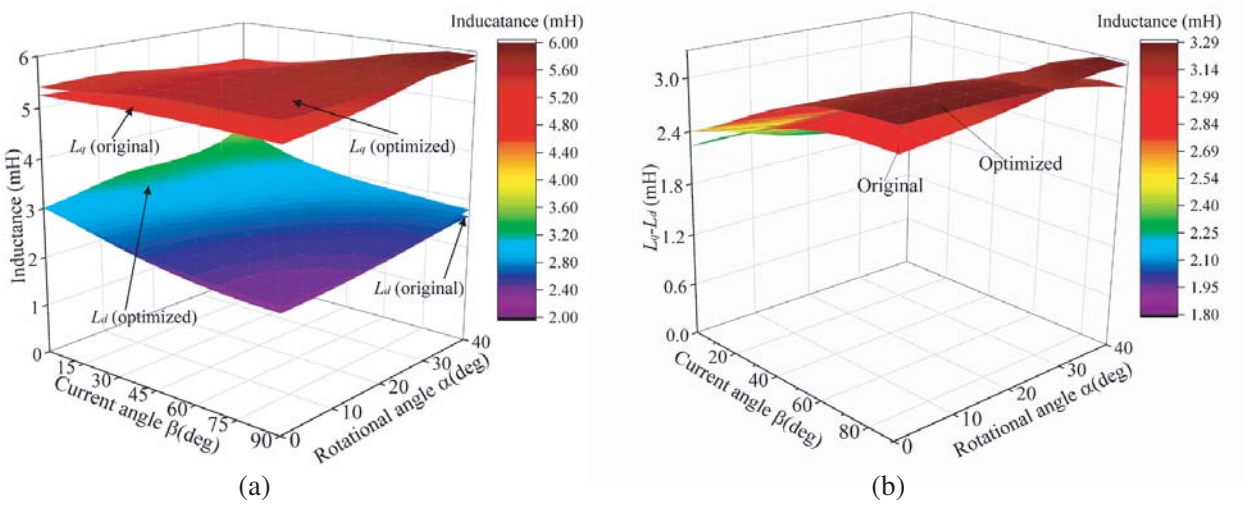

Figure 12. Comparison of inductance characteristics. (a) L_d and L_q. (b) Difference between L_q and L_d.

4.4. Torque Performances

Generally, the output torque of the motor can be expressed as:

$$T_{out} = \frac{3P}{2}\left[\psi_{pm} i_q + (L_d - L_q) i_d i_q\right] = \frac{3P}{2}\left[\psi_{pm} i_s \sin\beta + \frac{1}{2}(L_d - L_q) i_s^2 \sin 2\beta\right] \tag{9}$$

Figure 13 shows the torque performances of the original machine and optimized machine at rotational angle α of 0 deg. In Figure 13(a), the curves of torque-angle characteristics of the MFW-IPM machine are shown, and it can be seen that the peak value of the torque of the optimized machine is slightly larger than that of the original machine. The comparison of torque ripple in the MFW-IPM machine with the maximum torque operating condition is shown in Figure 13(b). It can be seen that the torque ripple of the optimized machine is about 12.8%, which is far less than that of the original machine of 26.8%. It means that the output torque performance of the optimized machine is better than that of the original machine.

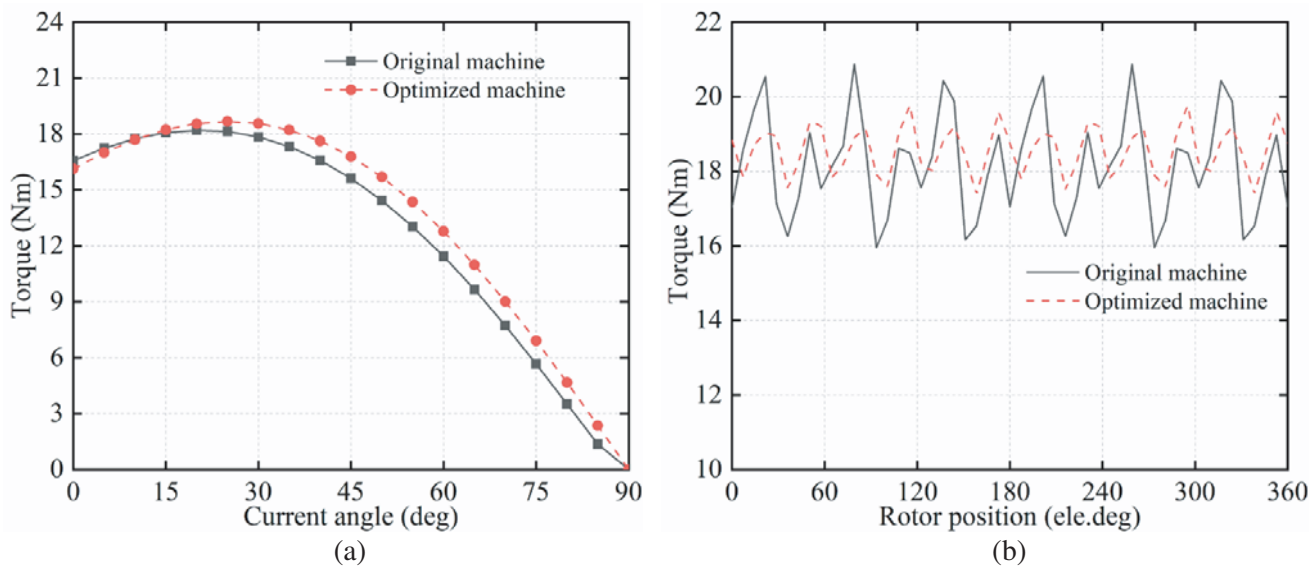

Figure 13. Comparison of torque characteristics under α of 0 deg. (a) Torque versus current angle. (b) Steady rated torque at the rated condition.

Based on the unique characteristics of the MFW-IPM machine, the output torque can be expressed as follows:

$$T_{out} = \frac{3P}{2}\left[\psi_{pm}(\alpha,\beta) i_s \sin\beta + \frac{1}{2}(L_d(\alpha,\beta) - L_q(\alpha,\beta)) i_s^2 \sin 2\beta\right] \tag{10}$$

According to Equation (10), the output torque of the MFW-IPM machine as a function of the current angle and the PM rotation angle is shown in Figure 14. As seen from the figure, the rate of torque decline of the optimized machine is larger than that of the original machine with the increase of rotational angle α. The maximum torque of the MFW-IPM machine is obtained at a larger current angle with the increase of rotational angle α. It is because the PM torque decreases, and the reluctance torque increases.

4.5. Flux-Weakening Ability and Speed Range

The proposed motor is designed to achieve a wider range of speeds, so it is necessary to study the flux weakening ability of the motor and the characteristics of torque and output power with the variation of speed.

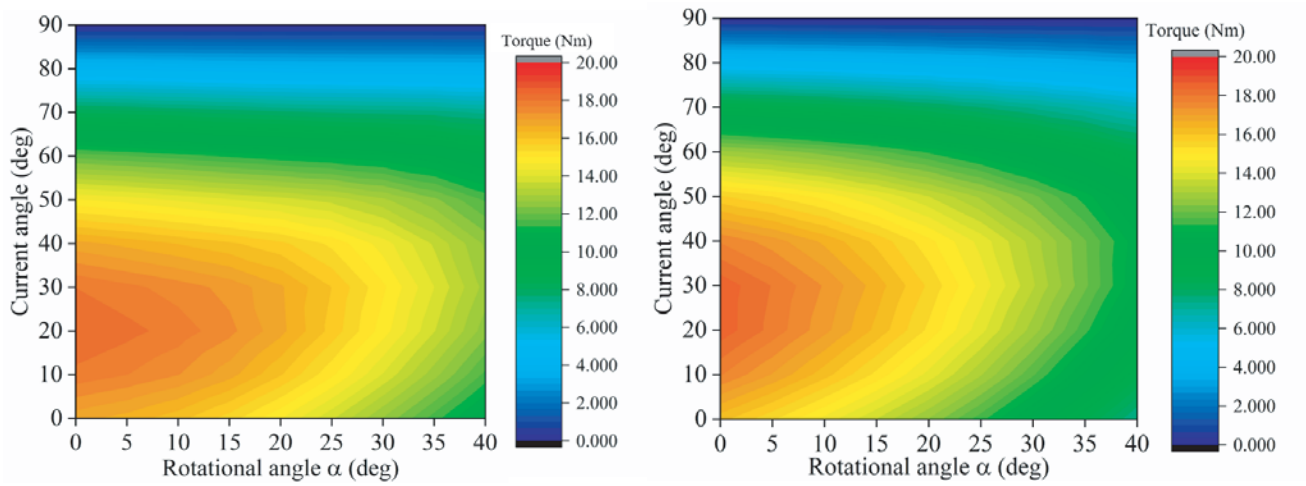

Figure 14. The output torque of the MFW-IPM machine as a function of current angle and PM rotation angle. (a) Original machine. (b) Optimized machine.

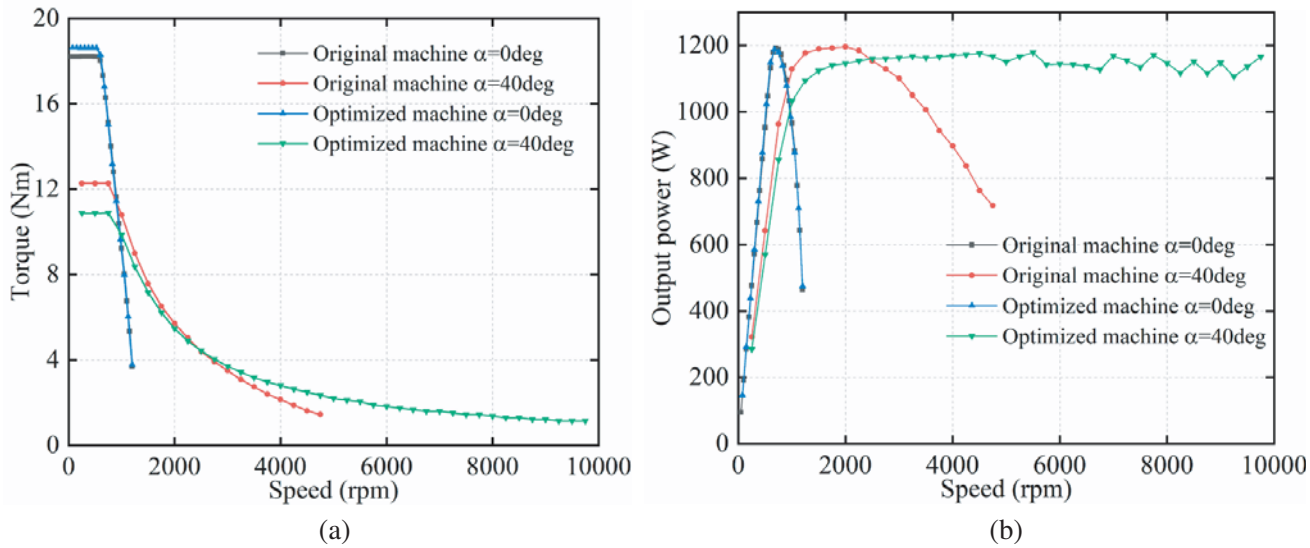

Figure 15. Torque-speed and output power-speed characteristics. (a) Torque-speed curves. (b) Output power-speed curves.

To indicate the flux-weakening capability, a factor K_{fw} can be defined as:

$$K_{fw} = \frac{L_d I_{lim}}{\psi_{pm}} \tag{11}$$

The flux-weakening coefficients of the original and the optimized machine under the different rotational angles α are listed in Table 5. It can be observed that the flux-weakening coefficient K_{fw} of the MFW-IPM machine increases with the increase of the rotational angle α. The flux-weakening coefficient of the optimized machine is higher than that of the original machine.

Figure 15 shows the torque-speed curves and output power-speed curves of the original and optimized machine. From the two figures, it can be seen that the speed range of the MFW-IPM machine widens with the increase of rotational angle α, and the speed range and constant power range of the optimized machine is wider than that of the original machine.

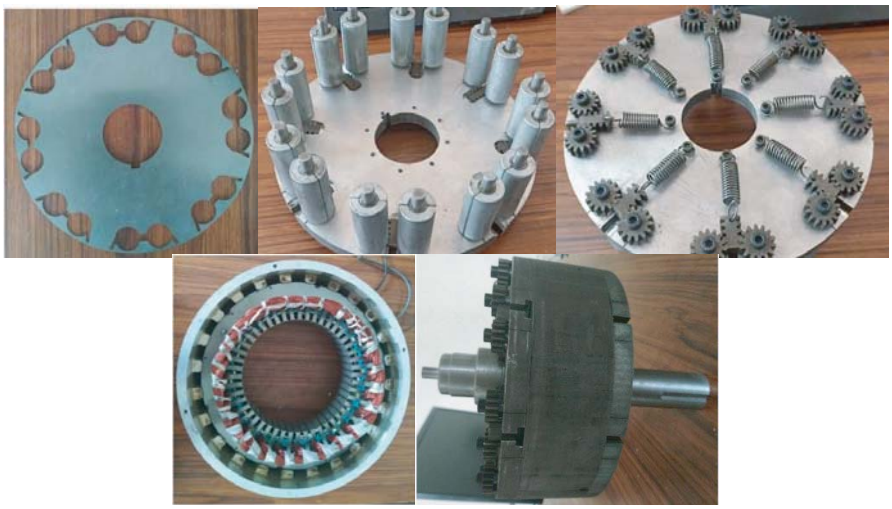

Figure 16. Prototype of the MFW-IPM machine.

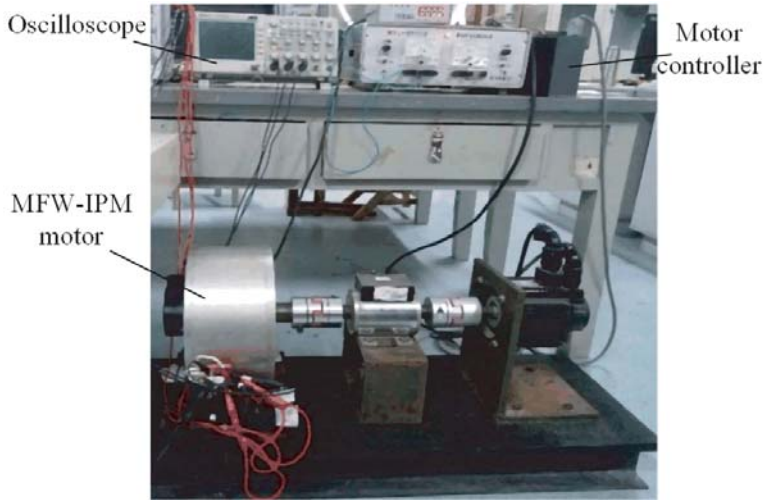

Figure 17. Experimental platform.

Table 5. Variation range of the design variables.

Machine	States	L_d (mH)	ψ_{pm} (Wb)	K_{fw}
Original machine	$\alpha = 0$ deg	2.45	0.104	0.589
	$\alpha = 40$ deg	2.63	0.067	0.981
Optimized machine	$\alpha = 0$ deg	2.56	0.104	0.615
	$\alpha = 40$ deg	2.84	0.051	1.391

5. EXPERIMENTAL VALIDATION

According to the optimization results, the MFW-IPM machine is manufactured. The rotor lamination, CPM, mechanical flux-adjusting device, stator, and prototype motor are shown in Figure 16. The

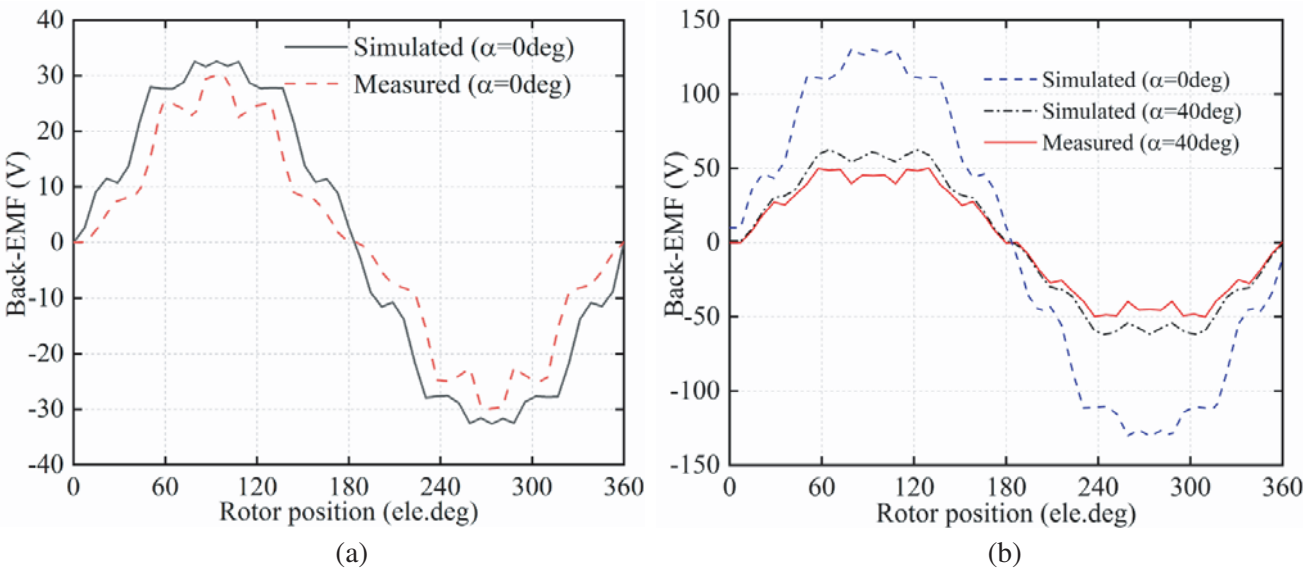

Figure 18. Comparison of no-load back-EMF. (a) Measured and simulated at 750 rpm. (b) With and without a mechanical flux-adjusting device at 3000 rpm.

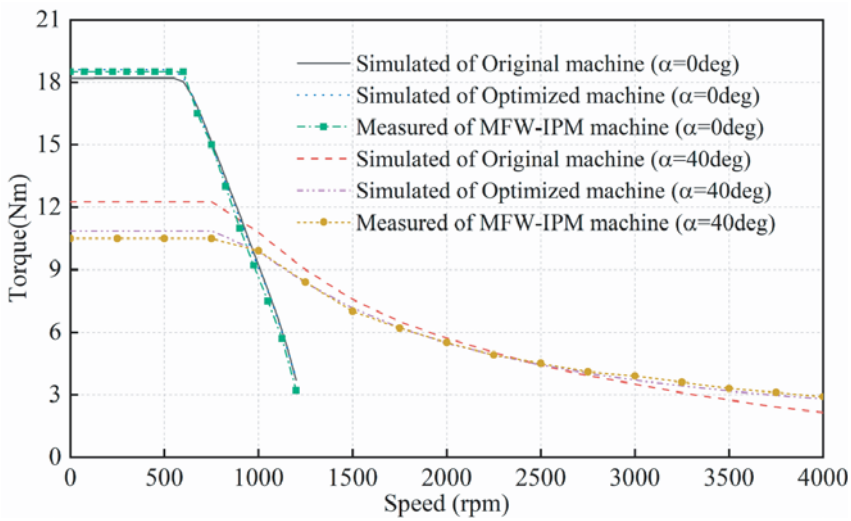

Figure 19. Torque versus speed.

corresponding experimental platform is shown in Figure 17. To better compare the results of FEA, the prototype motor is tested at rotation angles α of 0 deg and 40 deg. The comparison of measured and simulated of the no-load back-EMF waveforms of the MFW-IPM machine are shown in Figure 18. Figure 18(a) shows the no-load back EMF of the MFW-IPM machine at speed of 750 rpm. It can be seen that the measured value is slightly smaller than that of the simulated values, but the variation trends of the two waveforms are almost identical. Moreover, no-load back-EMF of the proposed machine with and without the mechanical flux-adjusting device (i.e., with ($\alpha = 40$ deg), without ($\alpha = 0$ deg)) at the speed of 3000 rpm is shown in Figure 18(b). As seen from the figure, the measured value is slightly smaller than that of the simulated values, and the no-load back-EMF of the MFW-IPM machine with the mechanical device is obviously smaller than that without the mechanical device. It is proved that the flux-weakening ability of the MFW-IPM machine can be improved by the mechanical device. Moreover, the simulated and measured torque-speed curves at different α states are shown in Figure 19. From

the figure, the measured torque-speed curve of the MFW-IPM machine is consistent with the simulated values of the optimized machine, and the performance of torque-speed is better than that of the original machine. It verifies the effectiveness of the motor design and optimization method.

6. CONCLUSION

In this paper, an MFW-IPM machine is optimized to realize a wider speed range. The topology and flux-adjusting principle of the proposed motor are introduced. To improve the overall performance of the MFW-IPM machine, the rotor structure of the motor is optimized. The sensitivity method is applied to evaluate the influence of each selected variable on the optimized objectives, where the optimized objectives include output torque, torque ripple, and flux-regulating ratio. Then, based on the sensitivity value, the design variables are divided into two layers, and the strong sensitivity is selected as the final design variables. The structural parameters of the motor are determined by the MOGA method. The electromagnetic performances of the original and optimized machines are compared, which confirms the effectiveness of the optimization method. Finally, the prototype motor is manufactured and tested. Both the simulation and test results verify that the flux-weakening ability of the proposed motor can be improved by the mechanical device.

ACKNOWLEDGMENT

This work was supported in part by the National Natural Science Foundation of China under grant No. 51767009 and 52067008, in part by the Plan Project of Jiangxi Province of P. R. China under grant No. 20181BAB206035, and in part by the Program of Qingjiang Excellent Young Talents, Jiangxi University of Science and Technology (JXUST).

REFERENCES

1. Wang, H. and S. Fang, "Design of new dual-stator field modulation machines," *IEEE Transactions on Industrial Electronics*, Vol. 67, No. 7, 5626–5636, 2020.
2. Chen, Q., G. Xu, F. Zhai, et al., "A novel spoke-type PM motor with auxiliary salient poles for low torque pulsation," *IEEE Transactions on Industrial Electronics*, Vol. 67, No. 6, 4762–4773, 2020.
3. Wang, D., X. Wang, and S. Jung, "Cogging torque minimization and torque ripple suppression in surface-mounted permanent magnet synchronous machines using different magnet widths," *IEEE Transactions on Magnetics*, Vol. 49, No. 5, 2295–2298, 2013.
4. Huynh, T. A. and M. Hsieh, "Comparative study of PM-assisted SynRM and IPMSM on constant power speed range for EV applications," *IEEE Trans. Magn.*, Vol. 53, No. 11, 1–6, 2017.
5. Amin, M. and G. A. A. Aziz, "Hybrid adopted materials in permanent magnet-assisted synchronous reluctance motor with rotating losses computation," *IEEE Trans. Magn.*, Vol. 55, No. 6, 1–5, 2019.
6. Wu, W., "Design and analysis of a new permeability-modulated interior permanent-magnet synchronous machine," *IEEE Trans. Magn.*, Vol. 57, No. 2, 1–5, 2021.
7. Jang, J., M. Humza, and B. Kim, "Design of a variable-flux permanent-magnet synchronous motor for adjustable-speed operation," *IEEE Trans. Ind. Appl.*, Vol. 52, No. 4, 2996–3004, 2016.
8. Ibrahim, M., L. Masisi, and P. Pillay, "Design of variable flux permanent-magnet machine for reduced inverter rating," *IEEE Trans. Ind. Appl.*, Vol. 51, No. 5, 3666–3674, 2015.
9. Sarigiannidis, A. G., M. E. Beniakar, and A. G. Kladas, "Fast adaptive evolutionary PM traction motor optimization based on electric vehicle drive cycle," *IEEE Trans. Veh. Technol.*, Vol. 66, No. 7, 5762–5774, 2017.
10. Liu, X., H. Chen, J. Zhao, et al., "Research on the performances and parameters of interior PMSM used for electric vehicles," *IEEE Trans. Ind. Electron.*, Vol. 63, No. 6, 3533–3545, 2016.
11. Zhao, X., S. Niu, and W. Fu, "Design of a novel parallel-hybrid-excited dual-PM machine based on armature harmonics diversity for electric vehicle propulsion," *IEEE Trans. Ind. Electron*, Vol. 66, No. 6, 4209–4219, 2019.

12. Giulii, F., G. De Donato Capponi, G. Borocci, et al., "Axial-flux hybrid-excitation synchronous machine: analysis, design, and experimental evaluation," *IEEE Trans. Ind. Appl.*, Vol. 50, No. 5, 3173–3184, 2014.
13. Zhang, L., X. Zhu, J. Gao, et al., "Design and analysis of new five-phase flux-intensifying fault-tolerant interior-permanent-magnet motor for sensorless operation," *IEEE Trans. Ind. Electron.*, Vol. 67, No. 7, 6055–6065, 2020.
14. Zhu, X., J. Huang, L. Quan, et al., "Comprehensive sensitivity analysis and multiobjective optimization research of permanent magnet flux-intensifying motors," *IEEE Trans. Ind. Electron.*, Vol. 66, No. 4, 2613–2627, 2019.
15. Zhao, X., B. Kou, L. Zhang, et al., "Design and analysis of permanent magnets in a negative-salient permanent magnet synchronous motor," *IEEE Access*, Vol. 8, No. 6, 182249–182259, 2020.
16. Limsuwan, N., T. Kato, K. Akatsu, et al., "Design and evaluation of a variable-flux flux-intensifying interior permanent-magnet machine," *IEEE Trans. Ind. Appl.*, Vol. 50, No. 2, 1015–1024, 2014.
17. Yu, C., J. Tamura, D. Reigosa, et al., "Position self-sensing evaluation of a FI-IPMSM based on high-frequency signal injection methods," *IEEE Trans. Ind. Appl.*, Vol. 49, No. 2, 880–888, 2013.
18. Yang, H., "Investigation of hybrid-magnet-circuit variable flux memory machines with different hybrid magnet configurations," *IEEE Trans. Ind. Appl.*, Vol. 57, No. 1, 340–351, 2021.
19. Yang, H., H. Zheng, Z. Q. Zhu, et al., "Comparative study of partitioned stator memory machines with series and parallel hybrid PM configurations," *IEEE Trans. Magn.*, Vol. 55, No. 7, 1–8, 2019.
20. Liu, G., G. Xu, W. Zhao, et al., "Improvement of torque capability of permanent-magnet motor by using hybrid rotor configuration," *IEEE Trans. Energy Convers.*, Vol. 32, No. 3, 953–962, 2017.
21. Du, Z. S. and T. A. Lipo, "Cost-effective high torque density Bi-magnet machines utilizing rare earth and ferrite permanent magnets," *IEEE Trans. Energy Convers.*, Vol. 35, No. 3, 1577–1584, 2020.
22. Lee, J. H., J. Kim, J. Song, et al., "Distance-based intelligent particle swarm optimization for optimal design of permanent magnet synchronous machine," *IEEE Trans. Magn.*, Vol. 53, No. 6, 1–4, 2017.
23. Sun, X., Z. Shi, G. Lei, Y. Guo, et al., "Multi-objective design optimization of an IPMSM based on multilevel strategy," *IEEE Trans. Ind. Electron.*, Vol. 68, No. 1, 139–148, 2021.
24. Liu, G., Y. Wang, Q. Chen, G. Xu, et al., "Multiobjective deterministic and robust optimization design of a new spoke-type permanent magnet machine for the improvement of torque performance," *IEEE Trans. Ind. Electron.*, Vol. 67, No. 12, 10202–10212, 2020.
25. Du, G., Q. Zhou, S. Liu, et al., "Multiphysics design and multiobjective optimization for high-speed permanent magnet machines," *IEEE Trans. Trans. Electr.*, Vol. 6, No. 3, 1084–1092, 2020.